Preparation of HKUST-1/PEI mixed-matrix membranes: adsorption-diffusion coupling control of small gas molecules

Yanjiao Wang, Ge Yang, Hailing Guo, Xianglong Meng, Guodong Kong, Zixi Kang, Rémy Guillet-Nicolas, Svetlana Mintova

Preparation of HKUST-1/PEI mixed-matrix membranes: adsorption-diffusion coupling control of small gas molecules

Yanjiao Wang [a,+], Ge Yang [a,b,+], Hailing Guo [a,*], Xianglong Meng [a], Guodong Kong [c], Zixi Kang [c], Rémy Guillet-Nicolas [d], Svetlana Mintova [a,d,*]

[a] State Key Laboratory of Heavy Oil Processing Key Laboratory of Catalysis, China National. Petroleum Corp. (CNPC) China University of Petroleum (East China) Qingdao 266555 (P.R. China).

[b] College of Science, China University of Petroleum (East China), Qingdao, Shandong, 266580, (PR China).

[c] School of Materials Science and Engineering, China University of Petroleum (East China), Qingdao, Shandong, 266580, (PR China).

[d] Laboratoire Catalyse et Spectrochimie (LCS), ENSICAEN, UNICAEN, CNRS, Normandie Université, 6 boulevard du Marechal Juin, 14050 Caen (France).

* Corresponding authors.

Email addresses: guohl@upc.edu.cn (H. Guo), mintova@ensicaen.fr (S. Mintova)

+ These authors contributed equally to this work.

Abstract

HKUST-1 nanocrystals (50-80 nm) were homogeneously dispersed in a polyetherimide (PEI) polymer matrix. The use of a capping agent (sodium formate)

prevented the agglomeration of HKUST-1 nanocrystals in the casting solution. The highly dispersed HKUST-1 nanocrystals were found to strengthen the interactions with the PEI and minimize the interfacial holes by providing more accessible Cu unsaturated metal sites for the C=O bonds on the five-membered rings of the PEI matrix. The PEI membrane loaded with 30 wt. % HKUST-1 nanocrystals (30-N-HKUST-1/PEI) showed a high H_2 permeability (193.3 Barrer at 25 °C under 1.5 bar) and good ideal H_2/CH_4 and H_2/CO_2 selectivity factor of 101.7 and 20.6 in a single gas test, respectively. In the gas mixture test, it also showed a good separation performance, i.e., a H_2/CH_4 and H_2/CO_2 selectivity factor of 82.4 and 16.5 was measured, respectively. The 30-N-HKUST/PEI membrane was tested in a gas mixture at different temperatures (25 - 100 °C), different pressures (0 - 3 bar) and various time (5 - 72 h) to study the performance in more realistic conditions thus to be further considered in the separation of syngas.

Keywords: HKUST-1 nanocrystals; capping agent; mixed-matrix membrane; interfacial defects; gas separation

Introduction

Metal organic frameworks (MOFs)/polymer mixed-matrix membranes (MMMs) have recently attracted much attention [1, 2] thanks to their growing interest for challenging gas separation/purification processes. These MMMs combine the advantages of MOFs' excellent physicochemical features with the high selectivity, desirable mechanical properties and economical processability of the polymer matrix [3, 4]. MOFs are made from an assembly of metal ions and organic linkers, which allow them to interact favorably with the bulk polymeric chain, thus achieving higher compatibility and avoiding the formation of micro-gaps [5, 6]. It is critical to control the noncovalent interactions and covalent bonds between the filler and polymer during the synthesis step in order to obtain a homogeneous dispersion within the polymeric matrix [7-9]. Adequate solvent dispersion and slight mechanical force is usually sufficient to avoid large agglomeration of MOF crystals in the suspension. Another method, which has been proven to effectively enhance the overall dispersion, consists of using MOF composites or MOFs modified by long-chain organic compounds as fillers. Finally, fine tuning of the particle morphology is also of importance for MOF-based membranes. MOF nanosheets [10], nanorods and nanoparticles [11] are often preferred because they provide larger interfacial areas at the MOF-polymer boundary interface, ultimately allowing a better integration.

It is important to improve the compatibility of the filler and the polymer matrix. One should not forget that the core of a MOFs-MMMs membrane process is the membrane material itself. Selecting the ideal MOF/polymer pair for a given separation process (e.g., hydrogen separation and purification) is not straightforward and include several parameters to be considered such as the durability, the mechanical integrity at operating conditions as well as the productivity and separation efficiency

to name only a few. Ultimately, the separation performance is always limited by the "trade-off" phenomenon between gas selectivity and permeability [12]. As summarized in Table. 1, numerous strategies have already been developed to improve MOFs-MMMs performance. These pioneering studies include the incorporation of MOFs with small pore size and high gas selectivity to fabricate MOFs-MMMs including PIM-1, 6FDA, Matrimid, PSf and PEI. Compared with the commercially available Matrimid and polyetherimide (PEI) membranes, the PIM-1 and 6FDA exhibit high permeability, but they do require expensive polymers that may hindered their industrial potential [13-17]. Therefore, cheap commercial polymers such as PEI, Matrimid and PSf appear as more attractive options for membrane separation processes, especially considering their exceptional chemical and physical properties. However, these polymers suffer from a low permeability. Here also, even if the combination of commercial polymers and MOFs can greatly improve this latter point, it remains that the choice of optimal filler and polymer materials is not really predictable and still highly relies on tedious trial and errors strategies [18-25]. Furthermore, several critical aspects regarding the design of MOFs hybrid membranes for an optimal gas separation mechanism, including solution-diffusion where performance is dominated by the polymer, size screening where fillers with small pore size regulate the performance, and Knudsen diffusion in which the large pore of the polymer and the filler control the separation process have been put forward and studied [3]. However, due to an insufficient characterization of the real pore structure and pore size distribution of experimental MOFs-MMMs, the relationship between structure and performance is not yet well understood and more research is urgently needed.

Herein, we propose a novel homogeneous MOFs-MMMs membranes based on

the combination of HKUST-1 nanocrystals and PEI. PEI, commercially known as ULTEM, is a high-performance thermoplastic polymer with imide, isopropylidene and ether groups [26, 27]. It is cheap, has a good chemical and heat resistance as well as a good processability. These features make it very suitable as a polymer matrix. However, as said above, membranes made from PEI polymers have a low permeability, far below the acceptable permeation performance for versatile operating conditions. To overcome this issue, inspired by previous studies on the high permeability of HKUST-1 in liquid separation [28, 29], we propose the addition of HKUST-1 fillers. It is a highly permeable MOF with a unit structure made of four carboxylic acid bridge forming a paddle-wheel structure. The main pore size is about 9 Å and its open three-dimensional architecture is expected to improve substantially the permeability of PEI membranes in gas separation. Meanwhile, the high adsorption CO_2 and CH_4 in of HKUST-1 is beneficial for selectivity improvement. Of particular importance, the Cu unsaturated metal sites of the MOF should favor the C=O bonds on the five-membered ring of the PEI polymer matrix, resulting in improved compatibility and homogeneity. HKUST-1 nanocrystals were prepared with the addition of a capping agent (sodium formate) which act as a chemical linker and prevent the agglomeration in suspension [30]. After sonication and stirring, the resulting highly dispersed HKUST-1 nanocrystals are thus uniformly dispersed in the Polyetherimide (PEI) polymer matrix. Finally, the MMM was scrapped with an automatic coating machine. The MMMs show high H_2 permeability and promising H_2/CO_2 and H_2/CH_4 selectivity. This behavior is attributed to (i) the controlled and homogeneous dispersion of HKUST-1 nanocrystals in PEI, and (ii) the favorable electrostatic interactions between HKUST-1 and PEI, which reduce the interface defects.

Table 1. State-of-the-art studies combining MOFs with polymer matrices.

Polymer	MOF				Permeability (Barrer)		Selectivity	ref
	Name	Pore size (nm)	Particle size	Loading (wt %)				
PIM-1	MOF-74	1.1	10-15 μm	20	11469.0 (H_2)	21269 (CO_2)	0.54	13
						1114.0 (CH_4)	10.3	
	ZIF-8	0.34	20-60 nm	28	10650.0 (H_2)	17050 (CO_2)	0.62	14
						1440 (CH_4)	7.4	
6FDA-DAM	ZIF-8	0.4-0.42	50-80 nm	23.8	899 (H_2)	41.2 (CH_4)	21.8	15
6FDA-Durene	ZIF-71	0.42	< 100 nm	30	4533.0 (H_2)	7750.0 (CO_2)	0.59	16
						813.0 (CH_4)	5.6	
6FDA-TP	ZIF-90	0.35	60-105 nm	50	179 (H_2)	63.0 (CO_2)	2.8	17
						1.8 (CH_4)	99.4	
Matrimid 5218	ZIF-8	0.34	50-150 nm	60	35.8 (H_2)	0.1 (CH_4)	358.2	18
	ZIF-8	0.34	≈60 nm	20	56.5 (H_2)	0.4 (CH_4)	157	19
	MIL-53	0.85	nanoscale	37	103.0 (H_2)	1.1 (CH_4)	93.6	20
	MOF-5	0.87	100 nm	30	53.8 (H_2)	20.2 (CO_2)	2.7	21
						0.5 (CH_4)	119.6	
Psf	MCM-41	0.85	2-4 μm	12/4	26.8 (H_2)	0.4 (CH_4)	67.0	23
	MIL-53		0.5-1 μm					
PEI	MOF-5	0.867	30-80 nm	5	14.09 (H_2)	2.3 (CO_2)	6.13	24
	ZIF-11	0.3	280 nm	20	27.1 (H_2)	6.95 (CO_2)	3.89	25
						0.32 (CH_4)	84.68	

2. Experiments

2.1. Materials

Copper (II) nitrate trihydrate ($Cu(NO_3)_2 \cdot 3H_2O$, 99.0 %-102 %) and sodium formate (HCOONa, ⩾99 %) were received from Sinopharm Chemical Reagent Co., Ltd. (China). Trimesic acid ($C_6H_3(CO_2H)_3$) and dichloromethane (CH_2Cl_2, analytical reagent) were provided by Shanghai Aladdin Biochemical Technology Co., Ltd. (China). Polyetherimide (PEI) was supplied by SABIC. Ethanol (CH_3CH_2OH, analytical reagent) was purchased from Tianjin Fuyu Fine Chemical Co., Ltd. (China). All chemicals were used as received without further treatment.

2.2. Synthesis of HKUST-1 nanocrystals and microcrystals

$Cu(NO_3)_2 \cdot 3H_2O$ (1.09 g) was dissolved in 36.0 mL of deionized water to form solution A. 1,3,5-Benzenetricarboxylic acid (0.63 g) and Sodium formate (0.94 g) were dissolved in another 36.0 mL of ethanol to form solution B. Then, solution B was poured into solution A under magnetic stirring (600 rpm) for 15 min and subjected to crystallization at 120 °C for 3 h. The product (denoted N-HKUST-1) was collected by centrifugation (5000 rpm, 15 min) and re-dispersed in deionized water (three times) and once in ethanol [31]. Finally, the N-HKUST-1 were freeze dried for 24 h. They were further dispersed in 5.0 mL of CH_2Cl_2 (MMMs solvent), and then treated prior membrane preparation (10 minutes mechanical stirring and 10 minutes sonication repeated three times). The crystals (denoted CH_2Cl_2-N-HKUST-1) were collected by centrifugation and freeze dried for 24 h. The synthesis process of HKUST-1 microcrystals is the same as that of nanocrystals, except that the dosage of sodium formate is reduced to 0.31g. Other conditions remain unchanged. The crystals (denoted M-HKUST-1) were collected by centrifugation and freeze dried for 24 h.

2.3. Preparation of HKUST-1-MMMs

The 5.0 wt % polymer solution was prepared by dissolving 0.25 g PEI in CH_2Cl_2 (5.0 mL) at room temperature until a clear yellowish uniform viscous solution was obtained. Different loadings of HKUST-1 were then dispersed in the above solution, following three rounds of 10-minute mechanical stirring and 10-minute sonication to ensure uniformity. The casting solutions were further scraped on a clean glass plate with an automatic coating machine to control the membrane thickness. After adequate evaporation of CH_2Cl_2 (at room temperature for 24 h, at 60 °C for 24 h, and at 120 °C for 24 h), the prepared HKUST-1/PEI MMMs were carefully peeled off from the glass plate. The loading amounts of N-HKUST-1 in the MMMs were 10.0 wt. %, 30 wt. % and 50.0 wt. %, which are denoted as 10-N-HKUST-1/PEI, 30-N-HKUST-1/PEI and 50-N-HKUST-1/PEI, respectively. The loading amounts of M-HKUST-1 in the MMMs were 30.0 wt. %, which are denoted as 30-M-HKUST-1/PEI. All the membranes were re-activated in vacuum oven at 120 °C for 24 h before gas permeability tests.

2.4. Characterization

HKUST-1 crystals and all the prepared MMMs were characterized by X-ray diffraction (XRD, Bruker, D8 Advance) at a scanning rate of 8° min^{-1} and 3-75° 2Theta range. The morphology and size of HKUST-1 crystals and the MMMs surface features were observed with a scanning electron microscope (SEM, JEOL-7900F). Fourier transform infrared spectroscopy (FT-IR) spectra were recorded using a Bruker Vertex 70V spectrometer with an average of 32 scans in the range 400-4000 cm^{-1}. The surface morphology of MMMs was characterized with atomic force microscopy (SHIMADZU, SMP-9700). X-Ray photoelectron spectroscopy (XPS) measurements were carried out on a PH 5000 Versaprobe spectrometer with a source gun of Al Kα.

N_2 sorption measurements were measured at 77 K using a Quantachrome, Autosorb IQ instrument. Prior to the measurements, the samples were degassed at 100 °C for 7 h under vacuum. The apparent surface area was calculated using the Brunauer-Emmet-Teller (BET) equation and following the procedure recommended by Rouquerol et al. for microporous sorbents [32]. Relevant pore size distributions were calculated from the adsorption branch of the isotherms by applying the kernel of (metastable) non-local density functional theory (NLDFT) adsorption isotherms considering an amorphous SiO_2 surface and a cylindrical pore model. Micro- and total pore volumes were also determined using the same kernel. The calculations were carried out using the ASiQwin 5.2 software provided by Quantachrome. Thermogravimetric analyses, TGA and DSC, were measured using a NETZSCH (STA 449 F5) analyzer under N_2 atmosphere from room temperature to 800 °C with a heating rate of 5 °C min^{-1}.

2.5. Gas-separation experiments

For the gas-separation measurement, the MMMs were placed in a stainless-steel cell and permeated to a steady state. The Wicke-Kallenbach technique was used to characterize the performance of one-component gas permeability and two-component mixed gas separation (1.5 bar upstream (feed gas) and 1 bar downstream (sweeping gas of argon (Ar)) with 0.5 bar transmembrane pressure drop). The membrane area tested was 0.785 cm^2. Gas feed was provided at 100 cm^3 min^{-1} (for mixture of gases, 100 cm^3 min^{-1} is the total flow of the two gases, i.e. 50 cm^3 min^{-1} for each gas), while the permeate side was swept by argon gas with a flow rate of 40 cm^3 min^{-1}. The permeated gas composition was determined using a gas chromatography (456-GC, Scion) equipped with a thermal conductivity detector (TCD). All the permeation

results were averaged from at least three different MMMs. The permeability, termed permeance P_i in Barrer (1 Barrer =1 × 10^{-10} cm^3(STP)·cm·$cm^{-2}s^{-1}$·$cmHg^{-1}$), of the MMMs was calculated with the following Equation (1):

$$P_i = \frac{10^{-10} l N_i}{A \Delta p_i} \qquad (1)$$

where N_i (cm^3(STP)·s^{-1}) is the permeate flow rate of component *i*, *l* (cm) is the thickness of membrane ΔP_i (cmHg) is the transmembrane pressure drop of component *i*, and *A* (m^2) is the membrane area.

The MMMs permselectivity was evaluated by the separation factor ($\alpha_{i/j}$), which was obtained according to Equation (2):

$$\alpha_{i/j} = \frac{X_i / X_j}{Y_i / Y_i} \qquad (2)$$

where *i*, *j* are the two components in the mixture and *X*, *Y* are the mole fractions in the permeate and feed solution, respectively.

Assuming that the gas transport processes through the 30-N-HKUST-1/PEI membrane are thermally activated, the E_{act} values can be calculated using the Arrhenius empirical equation (3):

$$\ln P = \frac{E_{act}}{RT} + C \qquad (3)$$

where *P* (Barrer) is the permeation coefficient, E_{act} (kJ/mol) corresponds to the activation energy of permeation.

The isotherms of 30-N-HKUST-1/PEI membrane at 273K and 298K were measured and the E_{ast} values can be calculated using the integral equation of Van't Hoff isovolumic equation (4):

$$\ln P = -\frac{E_{ast}}{R} \frac{1}{T} + C \qquad (4)$$

where P (Torr) is the adsorption equilibrium pressure, R is the gas constant, T (K) is the analysis temperature, E_{ast} (kJ/mol) corresponds to the heat of adsorption.

The E_{act} is related to the diffusion activation energy (ED) and heat of adsorption (E_{ast}) (5):

$$E_{act} = ED + E_{ast} \qquad (5)$$

3. Results and discussion

3.1 Characterization of HKUST-1 crystals

Sodium formate was used as an end-capping reagent to optimize both the shape and size of HKUST-1 crystals. Its addition results in fairly uniform bean-shaped nanocrystals with a crystal size of around 50-80 nm (Fig 1a) and sub microcrystals with crystal size of 300-500 nm (Fig 1b). The XRD diffraction pattern (Fig 2a) of the synthesized HKUST-1 crystals is in good agreement with the literature suggesting a proper phase purity [33] and a pristine MOF structure. The crystallite size of the N-HKUST-1 was calculated to be approximately 63 nm using the Scherer's equation (using all peaks), which is consistent with the SEM results. From the synthesis point of view, sodium formate allows to optimize the crystal morphology mainly from two aspects: (i) it reduces the average crystal size thanks to its modulating effect on the coordinating interactions between the metal ions and the organic linkers. Indeed, in the initial stage of the crystallization, sodium formate acts as a competitor of the organic linker BTC and coordinate to Cu cations. It results in an inhibited crystal growth and it allows more nuclei to be formed. (ii) This competitive coordination of the capping reagent appears to prevent the agglomeration of nanocrystals by

regulating the overall rate of crystal growth, ultimately leading to smaller and highly dispersed nanoparticles. The FTIR spectrum of as-synthesized HKUST-1 crystals is presented in Fig 2b. The typical bands found at 1375 cm^{-1}, 1564 cm^{-1} and 1644 cm^{-1} are attributed to the symmetrical vibrations of C-O, skeleton vibrations of the benzene and the stretching vibrations of the C=O, respectively.

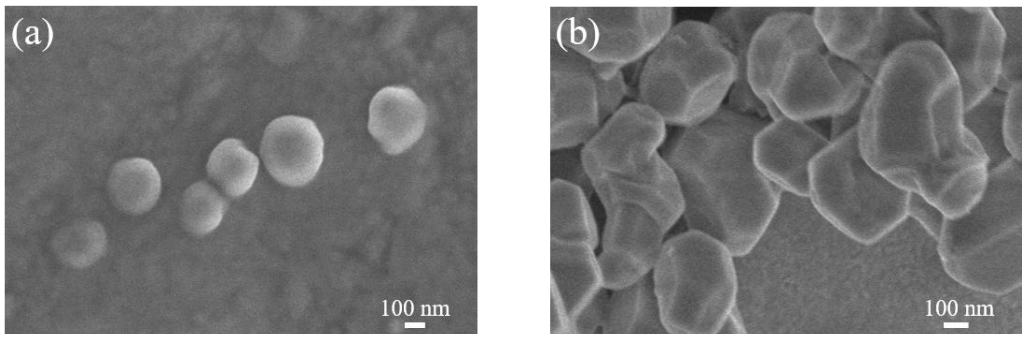

Fig 1. SEM pictures of (a) N-HKUST-1 and (b) M-HKUST-1

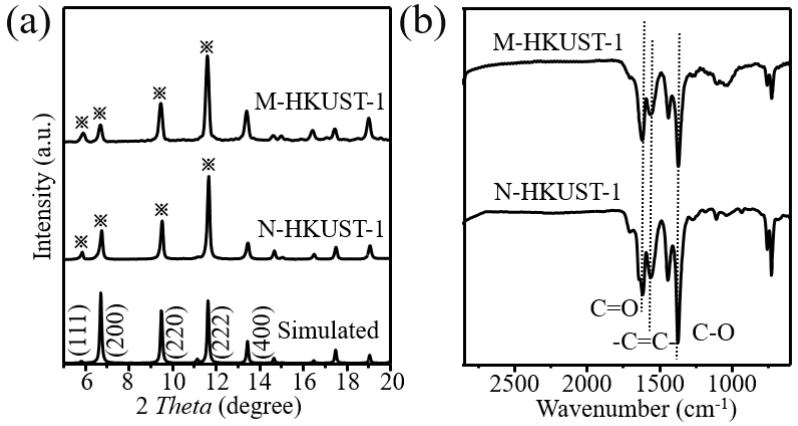

Fig 2. (a) XRD patterns and (b) FT-IR spectra of N-HKUST-1 and M-HKUST-1

Fig 3 exhibits the N_2 at 77 K adsorption-desorption isotherm of the MOF crystals. The HKUST-1 sample exhibits a hybrid type I/type IV isotherm that is nowadays commonly seen with modern micro/mesoporous (nano) materials. However, the main

component of the isotherm can be attributed to type I(a), being characteristic of microporous materials with pores below 1 nm. The isotherm also revealed a small H4 hysteresis loop indicative of the presence of intercrystalline mesoporosity (e.g. porosity present in-between nanocrystals) and a steep uptake at higher relative pressures (i.e., above P/P_0 = 0.98), typically associated with the presence of nanoparticles. A sharp and narrow pore size distribution with a mode pore size centered at around 0.8 nm (calculated using state-of-the-art NLDFT kernels), and a micropore volume of 0.45 cm^3g^{-1}cm were obtained (Table S1 and Fig 3). An apparent surface area, calculated using the BET model and verifying the Rouquerol's criteria for predominantly microporous samples, of 793 m^2/g and 667 m^2/g were determined for N-HKUST-1 and M-HKUST-1 respectively (Table S1), which is consistent with previously reported data [34]. All the physico-chemical data extracted from physisorption measurements confirmed the high-quality of the synthesized MOF sample. TGA curve of N-HKUST-1 and M-HKUST-1 are shown in Fig S1. The weight loss below 305 °C is attributed to the desorption of weakly physisorbed and confined water molecules, while the weight loss in the temperature range 305−365 °C arises from the release of coordinated water molecules. The MOF starts to degrade at 365 °C. In this region, the continuous weight loss originates from the decomposition of the organic linkers within the framework associated with a release of CO_2 up to ~750 °C.

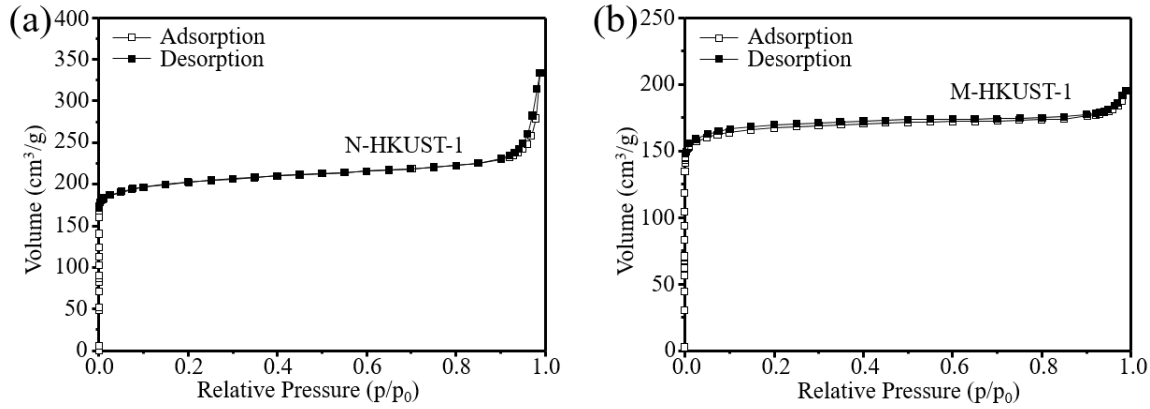

Fig 3. N_2 at 77 K physisorption isotherms of (a) N-HKUST-1 and (b) M-HKUST-1

Finally, in order to assess the stability and the suitability of the as-synthesized HKUST-1 crystals as a filler in the fabrication of MMM, CH_2Cl_2-N-HKUST-1 and CH_2Cl_2-M-HKUST-1 (MOF crystals treated three times with a 10-minute mechanical stirring and 10-minute sonication protocol) were also analyzed by XRD. The resulting pattern (Fig S2) shows that the crystal structure of HKUST-1 is perfectly maintained after this treatment, confirming the pertinence to use HKUST-1 crystals suspended in CH_2Cl_2 for fabricating MMMs.

3.2 Characterization of HKUST-1/PEI MMMs

A series of HKUST-1/PEI MMMs were prepared and the corresponding XRD patterns are shown in Fig 4. The pattern of the pure PEI membrane, exhibiting a broad peak centered at ~15° *2 Theta* is consistent with data reported in the literature [35, 36]. The XRD patterns of the different HKUST-1/PEI MMMs all exhibit the Bragg peaks representative of the HKUST-1. As expected, a gradual increase in the intensity of the peaks located at 5.8°, 6.7°, 9.5°, 11.7° and 13.5° is observed with an increase in the HKUST-1 crystals loading (Fig 4).

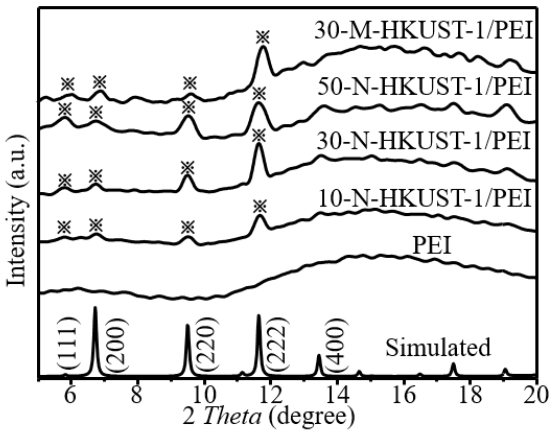

Fig 4. XRD patterns of pure PEI membrane and HKUST-1/PEI MMMs with different HKUST-1 loadings

The membrane forming process was further evaluated via optical imaging. As shown in Fig 5, all MMMs are of high-quality with an apparent homogeneous crystals dispersion and one can directly correlate the deepening of the blue color with the increasing of loading of HKUST-1 crystals. Of particular interest, SEM images, shown in Fig 6, revealed the textural differences in the MMMs. Indeed, while the surface of the pure PEI membrane is smooth (Fig 6a), the HKUST-1/PEI MMMs have a significant surface roughness which is increasing as a function of the particle's loading. The SEM pictures depicted in Fig 6b-d also confirmed the homogenous dispersion of the HKUST-1 nanocrystals. No obvious or major defects were found on the surface of the MMMs. The EDS results of Cu mapping also prove the homogeneous dispersion of HKUST-1 nanocrystals (Fig 6b-d) except for the 30-M-HKUST-1/PEI sample (see below). Such homogeneity is attributed to the use of the capping agent (sodium formate) during the synthesis which, as already said above, is believe to prevent the agglomeration of the MOF nanocrystals in suspension. From the cross-sectional views (Fig 7), the thickness of the PEI and HKUST-1/PEI MMMs

were determined to be 12.5–13.5 μm. These images revealed the polymer veins due to plastic deformation, which has also been found in other MOF-based MMMs. This effect is usually attributed to a strong interaction between the polymer and the filler [37] and will therefore result in a better integration and dispersion of the MOF filler within the host matrix. However, there are visible voids at the interfaces between the N-HKUST-1 and the polymer in the 50-N-HKUST-1/PEI membrane (Fig 7d). This result indicates an excessive loading of N-HKUST-1 resulting in irreversible damages in the PEI chain composing the polymer. According to the EDS results of the cross-section of the membrane, the Cu distribution in the N-HKUST-1/PEI MMMs is relatively homogeneous (Fig 7b-d). In the 30-M-HKUST-1/PEI membrane (Fig 7e), the agglomeration leads to inhomogeneous distribution of M-HKUST-1 as shown by EDS mapping. In addition, the larger size crystal also results in irreversible damages in the PEI chain composing the polymer. The surface morphology (Fig 8) and roughness (Table S2) of the HKUST-1/PEI MMMs were finally investigated by AFM. The average roughness of the HKUST-1/PEI MMMs increased substantially as compared with the one of the pristine PEI membrane, and became rougher with increasing loading of HKUST-1 crystals (Table S2). As illustrated in the TG curves (Fig 9), all HKUST-1/PEI MMMs are thermally stable up to 300 °C (initial weight loss being attributed to solvent), which make them suitable for gas separation applications.

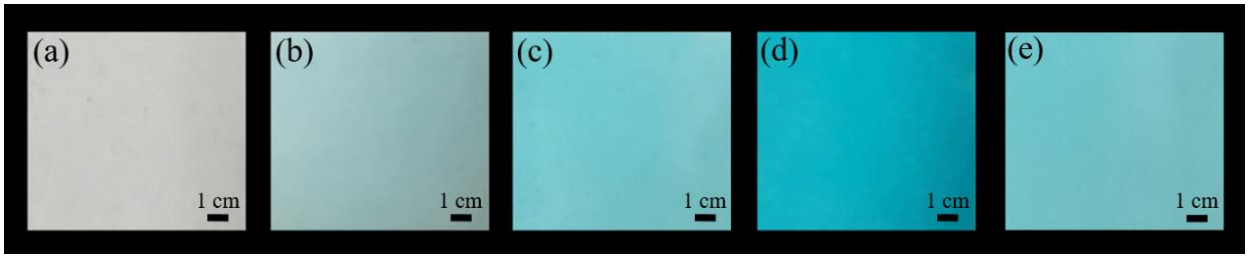

Fig 5. Optical images of (a) pure PEI membrane, (b) 10-N-HKUST-1/PEI, (c) 30-N-HKUST-1/PEI, (d) 50-N-HKUST-1/PEI and (e) 30-M-HKUST-1/PEI

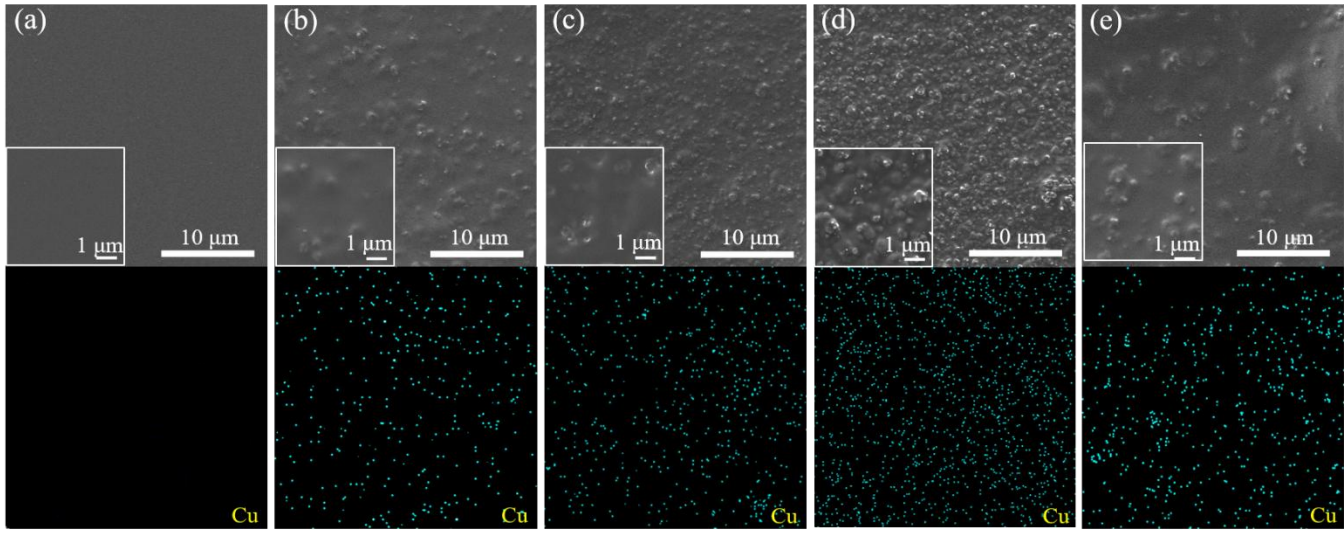

Fig 6. SEM images and EDS mapping of (a) pure PEI, (b) 10-N-HKUST-1/PEI, (c) 30-N-HKUST-1/PEI, (d) 50-N-HKUST-1/PEI and (e) 30-M-HKUST-1/PEI membranes

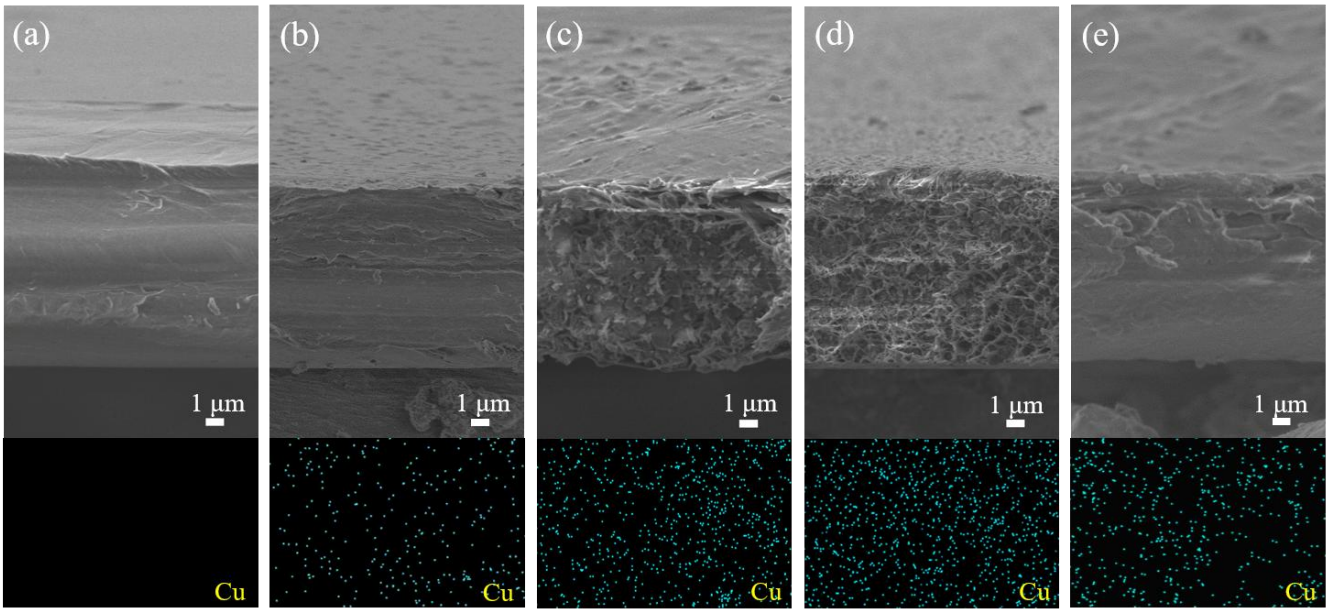

Fig 7. Cross-section SEM images and EDS mapping of (a) pure PEI, (b) 10-N-HKUST-1/PEI, (c) 30-N-HKUST-1/PEI, (d) 50-N-HKUST-1/PEI and (e) 30-M-HKUST-1/PEI membranes

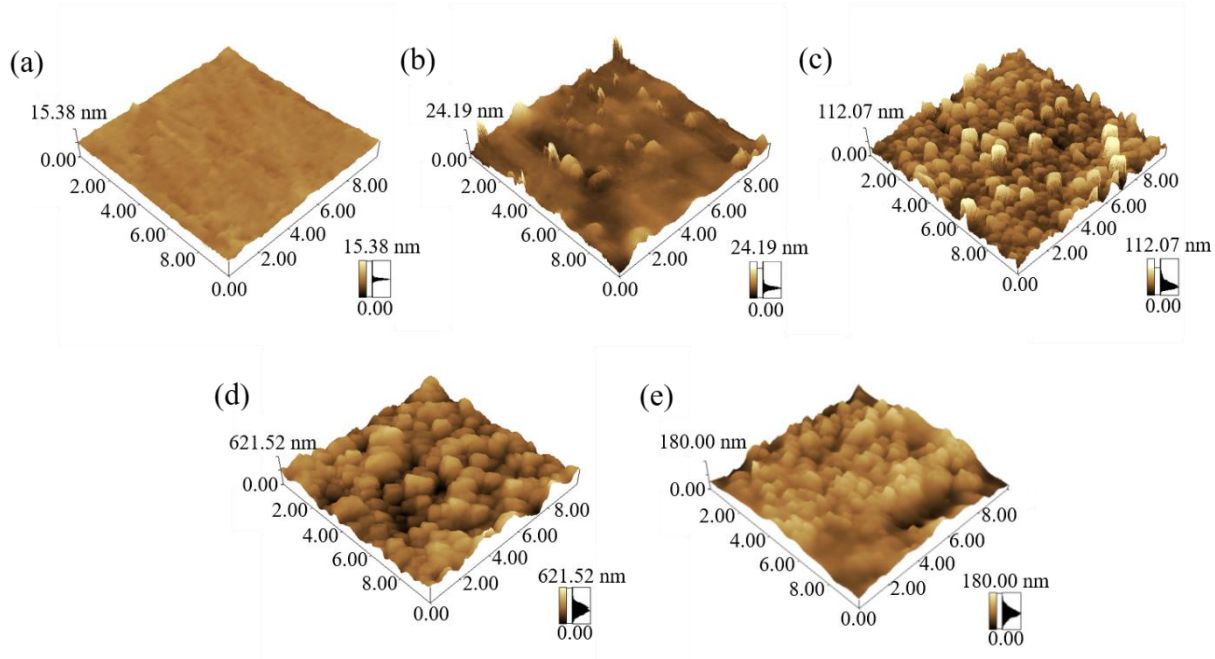

Fig 8. AFM images of (a) pure PEI, (b) 10-N-HKUST-1/PEI, (c) 30-N-HKUST-1/PEI, (d) 50-N-HKUST-1/PEI and (e) 30-M-HKUST-1/PEI membranes

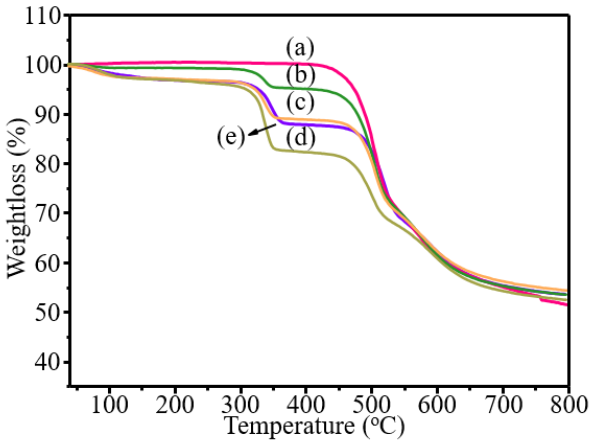

Fig 9. TG curves of (a) pure PEI, (b) 10-N-HKUST-1/PEI, (c) 30-N-HKUST-1/PEI, (d) 50-N-HKUST-1/PEI and (e) 30-M-HKUST-1/PEI membranes

The FTIR spectra of pure PEI membrane and HKUST-1/PEI MMMs are shown in Fig 10. The characteristic peaks coming from the PEI polymer can be clearly identified in all the different MOF/PEI MMMs. Namely, the peak at 1724 cm^{-1} and 1777 cm^{-1} can be attributed to the symmetric and asymmetric C=O stretching vibrations at the five-membered rings in PEI. The peaks at 1375 cm^{-1}, 1564 cm^{-1} and 1644 cm^{-1} belong to the symmetrical vibrations of C-O, skeleton vibrations of the benzene and the stretching vibrations of the C=O in HKUST-1, respectively, thus confirming the stable existence of N-HKUST-1 in the MMMs. It can also be noted that the intensity of the characteristic peak of N-HKUST-1 increases in accordance with the crystals loading. More important, an evident blue shift of the C=O peak in the FTIR spectra of the HKUST-1/PEI MMMs was observed (Fig 10b, from 1777 cm^{-1} to 1781 cm^{-1}). This result indicates an alteration in the electron distribution of the C=O group. It is suggested to originate from the action of the copper unsaturated metal sites in HKUST-1 onto oxygen atoms, making them more electronegative and resulting in a

tendency to withdraw the electron clouds of the chemical bonds. The existence of this electrostatic interaction was confirmed via XPS analysis (copper, Cu 2p) of N-HKUST-1 and 30-N-HKUST-1/PEI membrane (Fig 11). Compared to the N-HKUST-1, the binding energy for Cu $2p^{1/2}$ and Cu $2p^{3/2}$ shifted to the lower values for the 30-N-HKUST-1/PEI sample (from 954.8 eV to 953.2 eV and from 934.8 eV to 932.8 eV for Cu $2p^{1/2}$ and Cu $2p^{3/2}$, respectively), thus confirming that the density of the electron cloud near the copper unsaturated metal site increases. This is consistent with the results obtained by FTIR (Fig 10). To sum up, the copper unsaturated metal site interacts with the C=O of PEI polymer, reducing the binding energy of Cu $2p^{1/2}$ and Cu $2p^{3/2}$. This electrostatic interaction will therefore enhance the bonding strength of the PEI and the N-HKUST-1. As shown in Fig 12, these enhanced electrostatic interactions reduce the fluidity of PEI chains, ultimately leading to a higher glass transition temperature for the 30-N-HKUST-1/PEI membrane (213.8 °C) as compared to the pure PEI (208.5 °C) as shown in Fig 12, being consistent with all the previously discussed results.

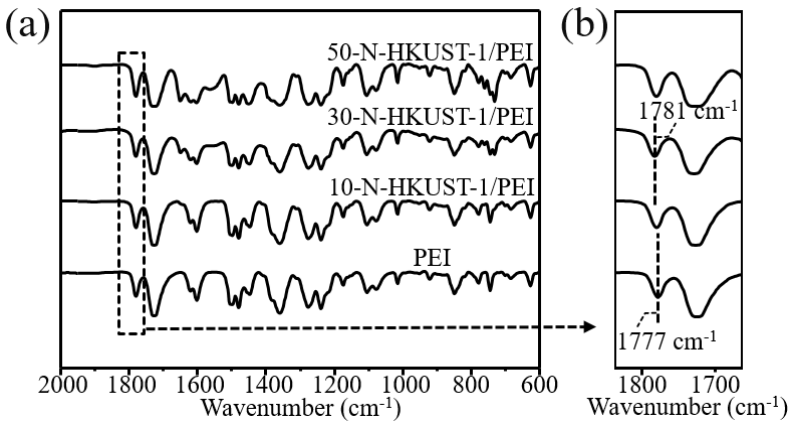

Fig 10. FTIR spectra of the pure PEI membrane and HKUST-1/PEI MMMs with different loading

amounts of N-HKUST-1 in the range (a) 600-2000 cm^{-1} and (b) 1600-1900 cm^{-1}

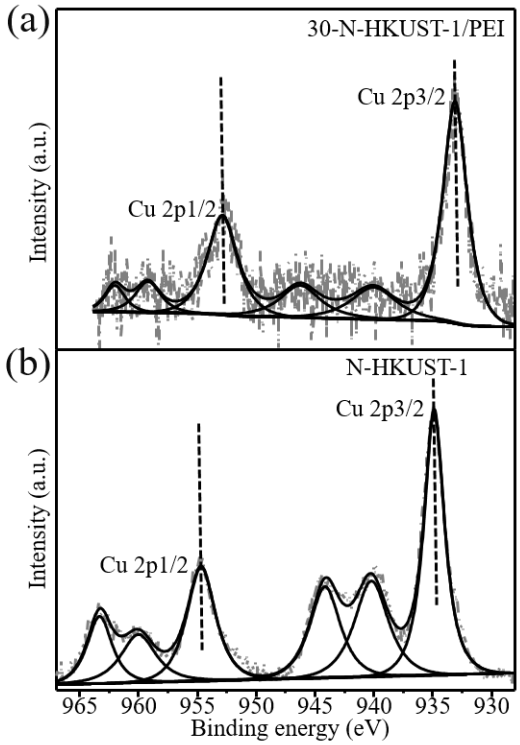

Fig 11. XPS spectra (Cu 2p) of (a) N-HKUST-1 and (b) 30-N-HKUST-1/PEI membranes

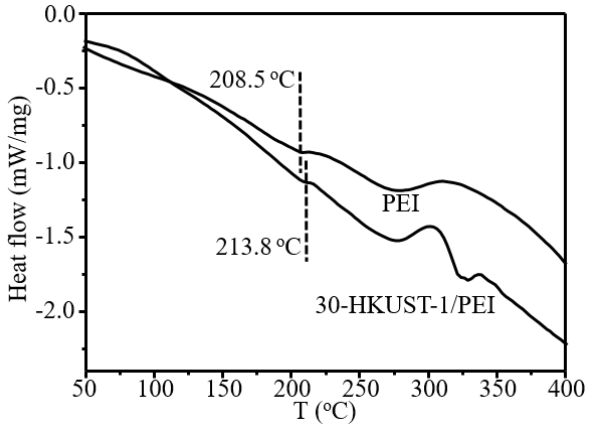

Fig 12. Differential scanning calorimetry (DSC) curves of pure PEI membrane and 30-N-HKUST-1/PEI membrane

3.3. Gas permeation measurements of HKUST-1/PEI MMMs

The single gas permeability of the pure PEI membrane and the HKUST-1/PEI MMMs were measured by the Wicke-Kallenbach technique at 25 °C and 1.5 bar. The

permeability and ideal selectivity values are summarized in Table S7, SI and Table 2. The HKUST-1/PEI MMMs exhibit a higher H_2 permeabilitiy as compared to the pure PEI membrane. Adding a 30 wt.% N-HKUST-1 to the PEI membrane resulted in a 2.55-fold increase in the H_2 permeability (75.8 barrer for pristine PEI membrane vs 193.3 barrer for 30-N-HKUST-1/PEI). This result can be rationalized by the intersecting three-dimensional pore network of the HKUST-1 embedded in PEI which provides faster and resistance-less through-pore channels for small and non-polar H_2 molecules (0.29 nm). On the contrary, the permeability of bigger gas molecules, such as CO_2 and CH_4 decreases due to their strong adsorption in the MOF nanocrystals. Indeed, the presence of Cu metal sites ensures a strong adsorption effect and a slow desorption of CO_2 and CH_4 in MOFs' channels, ultimately controlling their transport properties. Regarding the H_2/CO_2 and H_2/CH_4 ideal selectivity, among all the HKUST-1/PEI MMMs, the best ones were obtained for the 30-N-HKUST-1/PEI sample, being of 20.6 and 101.7, respectively. Quite remarkably, it represents a 5.7-fold increase as compared to the H_2/CO_2 ideal selectivity of the pure PEI membrane and 6.2-fold increase for the H_2/CH_4 one. In addition, the improved electrostatic interactions between the C=O bonds on the five-membered ring of PEI and the Cu^{2+} of HKUST-1 ensure a certain membrane's density with no loss of selectivity. However, it is to be noted that for the 50-N-HKUST-1/PEI membrane, with high loading of N-HKUST-1, the permeability of H_2, CO_2 and CH_4 increased and the H_2/CO_2 as well as the H_2/CH_4 ideal selectivity decreased. Here, the excessive amount of N-HKUST-1 in the PEI polymer matrix damaged the PEI chains, resulting

in the apparition of non-selective voids at the interface between the two materials, as shown in the SEM image (Fig 7d). Nevertheless, it remains that even with these voids, the CO_2 and CH_4 permeability of 50-N-HKUST-1/PEI was still lower than the pure PEI membrane, demonstrating the strong incorporation of HKUST-1 filler in MMMs. In addition, adding a 30 wt.% M-HKUST-1 to the PEI membrane resulted in a 8.62-fold increase in the H_2 permeability (75.8 barrer for pristine PEI membrane vs 529.2 barrer for 30-M-HKUST-1/PEI). The damages of the PEI chains induced by the larger crystal size of M-HKUST-1 and their inhomogeneous distribution lead to non-selective voids, ultimately resulting in a loss of selectivity (11.6 for H_2/CO_2 and 33.1 for H_2/CH_4) (Fig 7e).

Activation energy of permeation (E_{act}) values of 5.3 kJ/mol for H_2, 11.0 kJ/mol for CO_2 and 8.6 kJ/mol for CH_4 in single gas permeability were calculated for the best performing membrane, the 30-N-HKUST-1/PEI (Fig 13a and Table S3). The E_{act} of H_2 is extremely small due to the low diffusion resistance faced within the membrane, leading to fast diffusion of smaller H_2 molecules (0.29 nm) as compared to larger CO_2 (0.33 nm) and CH_4 (0.38 nm) ones. The calculated E_{ast} values are -0.6 kJ/mol for H_2, -25.4 kJ/mol for CO_2 and -11.2 kJ/mol for CH_4 through 273K and 298K isothermal adsorption test of 30-N-HKUST-1/PEI membrane (Fig 13b and Table. S4). Following Eq. 5, the calculated ED values are 5.9 kJ/mol for H_2, 36.4 kJ/mol for CO_2 and 19.8 kJ/mol for CH_4. The E_{ast} of CO_2 and CH_4 is much higher than the E_{ast} of H_2 due to the strong adsorption of these molecules by the HKUST-1 crystals. This effect can be attributed to the presence of Cu unsaturated metal sites in the MOF. Through carefully

comparing E_{ast} and ED of H_2, CO_2 and CH_4, the permeation of CO_2 and CH_4 is dominated by adsorption phenomena, while the permeation of H_2 is dominated by diffusion ones. The adsorption capacity of CO_2 in HKUST-1 is stronger than that of CH_4, which is also the reason why the permeation of CO_2 is higher than that of CH_4. Finally, the single gas separation performance of the 30-N-HKUST-1/PEI was found to outperform the well-known Robeson's upper bound (Fig S3) confirming the potential of N-HKUST-1 for the preparation of effective and economically relevant PEI-based MMMs.

Table 2. Gas permeability and ideal selectivity of pure PEI and HKUST-1/PEI MMMs at 25 °C and 1.5 bar

Membrane	**Gas Permeability (Barrer)**			**Ideal selectivity (α)**	
	H_2	CO_2	CH_4	H_2/CO_2	H_2/CH_4
Pure PEI	75.8	21.2	4.6	3.6	16.5
10-N-HKUST-1/PEI	120.8	11.2	2.7	10.8	44.7
30-N-HKUST-1/PEI	193.3	9.4	1.9	20.6	101.7
50-N-HKUST-1/PEI	241.8	19.3	4.1	12.5	59.0
30-M-HKUST-1/PEI	529.2	45.8	17.0	11.6	31.1

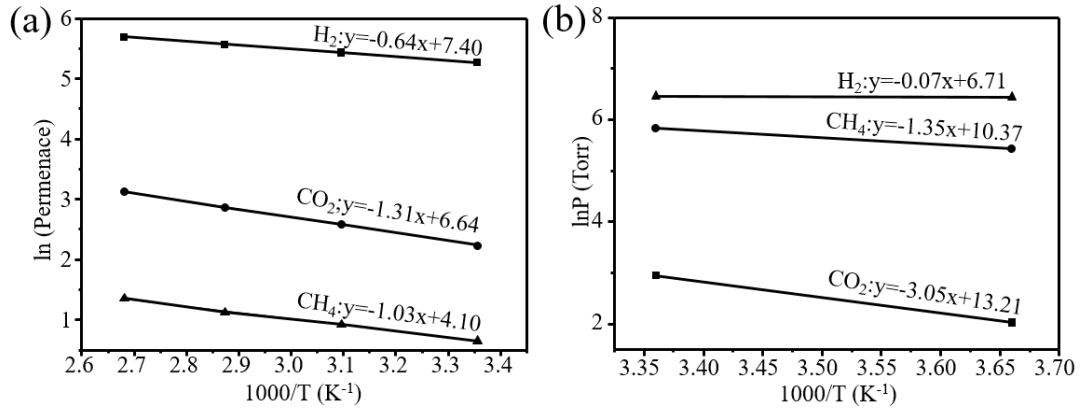

Fig 13. (a) Arrhenius temperature dependence of H_2, CO_2 and CH_4 permeances for the 30-N-HKUST-1/PEI membrane; (b) Van't Hoff plots of H_2, CO_2, and CH4 recorded at 273 K and 298 K

Finally, the H_2/CO_2 and H_2/CH_4 mixed gas permeation of HKUST-1/PEI MMMs were evaluated. As summarized in Table 3, a similar trend as the one found for single gas permeation was obtained. Focusing on 30-N-HKUST-1/PEI, while a slight decrease of the H_2 permeability (from 193.3 barrer to 136.8 barrer and 189.6 barrer in H_2/CO_2 and H_2/CH_4, respectively) was found due to the competitive permeation mechanism [38], the CO_2 and CH_4 permeability did not change significantly (from 9.4 barrer to 8.3 barrer and from 1.9 barrer to 2.3 barrer, respectively). A slight decrease in the H_2/CO_2 and H_2/CH_4 selectivity (16.5 and 82.4) was also noted.

Industrial syngas usually contains H_2, CO_2, CH_4, and their separation play a critical role in many synthesis and valorization processes. To further explore the "realistic" performance of 30-N-HKUST-1/PEI membrane in this separation, it was tested at different temperatures (25-100 $^{\circ}$C) (Table. S5) and pressures (0-3 bar) (Table. S6) under mixed gas permeation. As shown in Fig 14 and Fig 15, an increase in the

temperature and pressure resulted in a gradual increase of the permeability of H_2, CO_2 and CH_4. Under such conditions an induced desorption of CO_2 and CH_4 is observed [39]. The same effect explains the loss of selectivity even for 30-N-HKUST-1/PEI membrane, it remains much higher than the one of pure PEI. In addition, the stability test (72 h) revealed that the permeability and selectivity of the 30-N-HKUST-1/PEI membrane remains unchanged (Fig 16). Our results clearly demonstrate the potential of the MOF/PEI MMMs for practical applications in harsh conditions as well as continuous and extended on-stream time.

Table 3. Mixed gas permeation (H_2/CO_2 and H_2/CH_4) results of the PEI and HKUST-1/PEI MMMs at 25 °C and 1.5 bar

Membrane	**Gas Permeability (Barrer)**		**Selectivity (α)**	**Gas Permeability (Barrer)**		**Selectivity (α)**
	H_2	CO_2	H_2/CO_2	H_2	CH_4	H_2/CH_4
Pure PEI	56.0	23.7	2.4	58.3	4.3	13.6
10-N-HKUST-1/PEI	98.6	14.1	7.0	109.0	3.6	30.3
30-N-HKUST-1/PEI	136.8	8.3	16.5	189.6	2.3	82.4
50-N-HKUST-1/PEI	176.2	27.7	6.4	202.0	5.0	40.4

30-M-HKUST-1/PEI	482.7	36.6	13.2	498.8	24.1	20.7

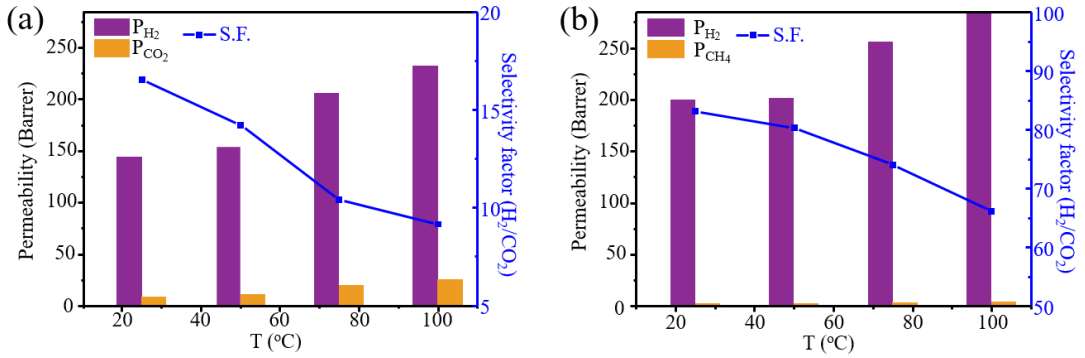

Fig 14. (a) Permeability and separation (H_2/CO_2) of 30.0-HKUST-1/PEI membrane at different temperatures (25 – 100 °C); (b) Permeability and separation (H_2/CH_4) of 30.0-HKUST-1/PEI membrane at different temperatures (25 – 100 °C)

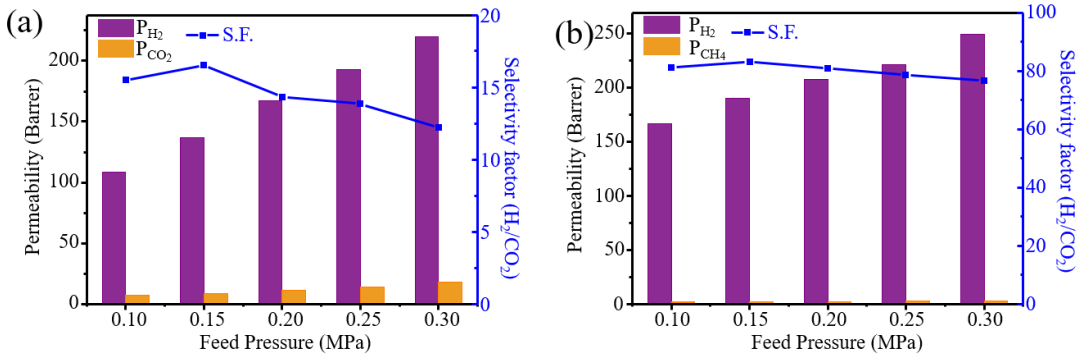

Fig 15. (a) Permeability and separation (H_2/CO_2) of 30.0-HKUST-1/PEI membrane at different feed pressure (0.10 – 0.30 MPa); (b) Permeability and separation (H_2/CH_4) of 30.0-HKUST-1/PEI membrane at different temperatures (0.10 – 0.30 MPa)

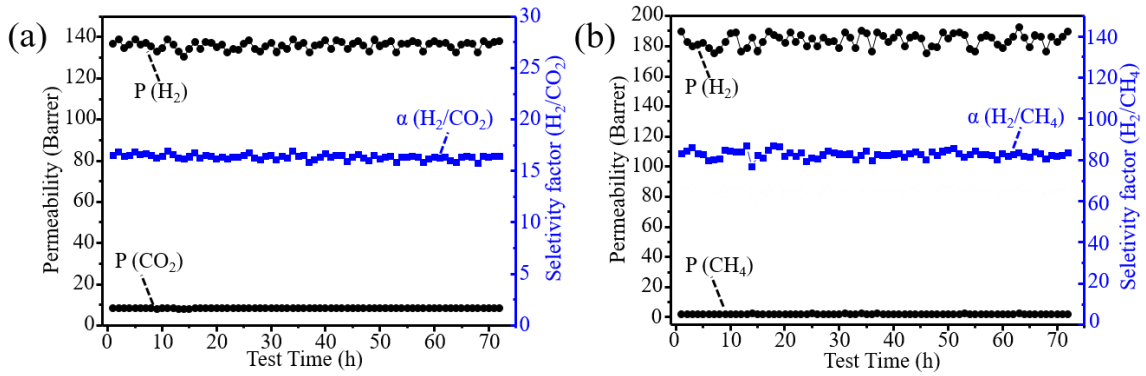

Fig 16. Stability of 30-N-HKUST-1/PEI membrane in (a) H_2/CO_2 and (b) H_2/CH_4 mixed gas separation tests performed continuously for 72 hours

4. Conclusions

Mixed matrix membranes were prepared by deposition of various amount of HKUST-1 nanocrystals (50-80 nm) in the polyetherimide matrix. The agglomeration of the HKUST-1 nanocrystals in the coating suspension was eliminated by using a capping agent (sodium formate). The MMMs show high H_2 permeability and H_2/CO_2 and H_2/CH_4 selectivity. This is attributed to the homogeneous dispersion of HKUST-1 nanocrystals in the PEI and the electrostatic interaction between the HKUST-1 nanocrystals and PEI, which reduced the interface defects. The optimum H_2 permeability (193.3 barrer) and ideal selectivity (20.6 in H_2/CO_2 and 101.7 in H_2/CH_4) are obtained for the 30-N-HKUST-1/PEI membrane. According to the energy calculation, an adsorption-diffusion coupling separation mechanism is proposed. The exceptional gas separation performance along with the high stability of the MMMs render them attractive for hydrogen separation application.

Declaration of Competing Interest

The authors declare that they have no known competing financial interests or personal relationships that could have appeared to influence the work reported in this paper.

Acknowledgements

This work is supported by the National Natural Science Foundation of China (Grant No. U1862118，No. 21975285, No.21991091, No. 21991090), the Fundamental Research Funds for the Central Universities (No. 21CX06024A), and the Sino-French International Associated Laboratory LIA “Zeolite”.

References

[1] T. Kitao, Y. Zhang, S. Kitagawa, Hybridization of MOFs and polymers, Chem. Soc. Rev. 46 (2017) 3108-3133. http://dx.doi.org/10.1039/c7cs00041c.

[2] R. Lin, B.V. Hernandez, G. Lei, Metal organic framework based mixed matrix membranes: an overview on filler/polymer interfaces, J. Mater. Chem. A. 6 (2018) 293-312. https://doi.org/10.1039/C7TA07294E.

[3] Q. Qian, P.A. Asinger, M.A. Lee, MOF-Based Membranes for Gas Separations, Chem. Rev. 120 (2020) 8161-8266. http://dx.doi.org/10.1021/acs.chemrev.0c00119.

[4] Y. Lv, L. Ma, F. Svec, Engineering of filler/polymer interface in metal rganic framework-based mixed atrix membranes to enhance gas separation, Chem. Asian. J. 20 (2019) 3502-3514. http://dx.doi.org/10.1002/asia.201900843.

[5] Y. Cheng, Z. Wang, D. Zhao. Mixed Matrix Membranes for Natural Gas

Upgrading: Current Status and Opportunities, Ind. Eng. Chem. Res. 57 (2018) 4139-4169. https://doi.org/10.1021/acs.iecr.7b04796.

[6] H.T. Jeazet, C. Staudt, C. Janiak. Metal-organic frameworks in mixed-matrix membranes for gas separation, Dalton. Trans. 41 (2012) 14003-14027. https://doi.org/10.1039/c2dt31550e.

[7] D.Q. Vu, W.J. Koros, S.J. Miller, Mixed matrix membranes using carbon molecular sieves: I. Preparation and experimental results, J. Membr. Sci. 211 (2003) 311–334. http://dx.doi.org/10.1016/s0376-7388(02)00429-5.

[8] D.Q. Vu, W.J. Koros, S.J. Miller, Effect of condensable impurity in CO_2/CH_4 gas feeds on performance of mixed matrix membranes using carbon molecular sieves, J. Membr. Sci. 221 (2003) 233–239. http://dx.doi.org/10.1016/S0376-7388(02)00429-5.

[9] M. Anson, J. Marchese, E. Garis, N. Ochoa, C. Pagliero, ABS copolymer-activated carbon mixed matrix membranes for CO_2/CH_4 separation, J. Membr. Sci. 243 (2004) 19-28. http://dx.doi.org/10.1016/j.memsci.2004.05.008.

[10] S. Feng, M. Bu, J. Pang, Hydrothermal stable ZIF-67 nanosheets via morphology regulation strategy to construct mixed-matrix membrane for gas separation, J. Membr. Sci. 593 (2020) 7376-7388. https://doi.org/10.1016/j.memsci.2019.117404.

[11] A. Sabetghadam, B. Seoane, D. Keskin, Metal Organic Framework Crystals in Mixed-Matrix Membranes: Impact of the Filler Morphology on the Gas Separation Performance, Adv. Funct. Mater. 26 (2016) 3154-3163.

http://dx.doi.org/10.1002/adfm.201505352.

[12] L.M. Robeson, The upper bound revisited, J. Membr. Sci. 320 (2008) 390-400. http://dx.doi.org/10.1016/j.memsci.2008.04.030.

[13] N. Tien-Binh, H. Vinh-Thang, X.Y. Chen, Crosslinked MOF-polymer to enhance gas separation of mixed matrix membranes, J. Membr. Sci. 520 (2016) 941-950. http://dx.doi.org/10.1016/j.memsci.2016.08.045.

[14] A.F. Bushell, M.P. Attfield, C.R. Mason, Gas permeation parameters of mixed matrix membranes based on the polymer of intrinsic microporosity PIM-1 and the zeolitic imidazolate framework ZIF-8, J. Membr. Sci. 427 (2013) 48-62. http://dx.doi.org/10.1016/j.memsci.2012.09.035.

[15] Z. Chen, R.P. Lively, K. Zhang, Unexpected Molecular Sieving Properties of Zeolitic Imidazolate Framework-8, J. Phys. Chem. Lett. 3 (2012) 2130-2134. http://dx.doi.org/10.1021/jz300855a.

[16] S. Japip, H. Wang, Y. Xiao, Highly permeable zeolitic imidazolate framework (ZIF)-71 nano-particles enhanced polyimide membranes for gas separation, J. Membr. Sci. 467 (2014) 162-174. http://dx.doi.org/10.1016/j.memsci.2014.05.025.

[17] Q. Zhang, S. Luo, J.R. Weidman, Preparation and gas separation performance of mixed-matrix membranes based on triptycene-containing polyimide and zeolite imidazole framework (ZIF-90), Polymer. 131 (2017) 209-216. http://dx.doi.org/10.1016/j.polymer.2017.10.040.

[18] C.M. Josephine, K.J. Balkus, J.P. Ferraris, Molecular sieving realized with

ZIF-8/Matrimid mixed-matrix membranes, J. Membr. Sci. 361 (2010) 28-37. http://dx.doi.org/10.1016/j.memsci.2010.06.017.

[19] Q. Song, S.K. Nataraj, M.V. Roussenova, Zeolitic imidazolate framework (ZIF-8) based polymer nanocomposite membranes for gas separation, Energ. Environ. Sci. 5 (2012) 8359-8369. http://dx.doi.org/10.1039/C2EE21996D.

[20] J.O. Hsieh, K.J. Balkus, J.P. Ferraris, MIL-53 frameworks in mixed-matrix membranes, Micropor. Mesopor. Mat. 196 (2014) 165-174. http://dx.doi.org/10.1016/j.micromeso.2014.05.006.

[21] E.V. Perez, K.J. Balkus, J.P. Ferraris, Mixed-matrix membranes containing MOF-5 for gas separations, J. Membr. Sci. 328 (2009) 165-173. http://dx.doi.org/10.1016/j.memsci.2008.12.006.

[22] M. Valero, B. Zornoza, C. Téllez, Mixed matrix membranes for gas separation by combination of silica MCM-41 and MOF NH2-MIL-53(Al) in glassy polymers. Micropor. Mesopor. Mat. 192 (2014) 23-28. http://dx.doi.org/10.1016/j.micromeso.2013.09.018.

[23] A. Mehrzad, P. Majid, Mixed matrix membranes incorporated with cubic-MOF-5 for improved polyetherimide gas separation membranes: Theory and experiment, J. Ind. Eng. Chem. 20 (2014) 3857-3868. http://dx.doi.org/10.1016/j.jiec.2013.12.091.

[24] M.A. Borolu, Structural characterization and gas permeation proper ties of polyetherimide (PEI)/zeolitic imidazolate (ZIF-11) mixed matrix membranes,Turk. J. Chem. 2 (2016) 183-206.

http://dx.doi.org/10.18596/jotcsa.62047.

[25] E.G. Ayman, F. Eric, R. Denis, Asymmetric Polyetherimide Membranes (PEI) for Nanofiltration Treatment, Eur. Polym. J. 105 (2018) 204-216. https://doi.org/10.1016/j.eurpolymj.2018.06.001.

[26] S.A. Hashemifard, A.F. Ismail, T. Matsuura, Effects of montmorillonite nano-clay fillers on PEI mixed matrix membrane for CO_2 removal, Chem. Eng. J. 170 (2011) 316-325. https://doi.org/10.1016/j.cej.2011.03.063.

[27] G. Yang, H.L. Guo, S. Mintova, Green Hydrogen Separation from Nitrogen by Mixed-Matrix Membranes Consisting of Nanosized Sodalite Crystals, ChemSusChem. 12 (2019) 4529-4537. https://doi.org/10.1002/cssc.201802577.

[28] C.Y. Chuah, S.Samarasinghe, L. Wen, Leveraging Nanocrystal HKUST-1 in Mixed-Matrix Membranes for Ethylene/Ethane Separation, Membranes. 10 (2020) 74. https://doi.org/10.3390/membranes10040074.

[29] Y. Lin, H.C. Wu, T. Yasui, T. Yoshioka, H. Matsuyama, Development of HKUST-1 nanofiller-templated polyethersulfone (PES) mixed matrix membrane for highly-efficient ultrafiltration process, ACS. Appl. Mater. Inter. 11 (2019) 18782-18796. https://doi.org/10.1021/acsami.9b04961.

[30] H. Guo, G. Zhu, I.J. Hewitt, Twin Copper Source" Growth of Metal-Organic Framework Membrane: $Cu_3(BTC)_2$ with High Permeability and Selectivity for Recycling H_2, J. Am. Chem. Soc. 131 (2019) 1646-1647. http://dx.doi.org/10.1021/ja8074874.

[31] H. Guo, Y. Zhu, W. Song, Combining Coordination Modulation with Acid–Base

Adjustment for the Control over Size of Metal–Organic Frameworks, Chem. Mater. 24 (2012) 444–450. http://dx.doi.org/10.1021/cm202593h.

[32] J. Rouquerol, F. Rouquerol, P. Llewellyn, Adsorption at the Gas-Solid and Liquid-Solid Interface, Elsevier Scientific Pub, The Kingdom of the Netherlands, 1982.

[33] Y.Q. Lin, H.C. Wu, T. Yasui, Development of HKUST-1 nanofiller-templated polyethersulfone (PES) mixed matrix membrane for highly-efficient ultrafiltration process, ACS. Appl. Mater. Inter. 11 (2019) 18782-18796. http://dx.doi.org/10.1021/acsami.9b04961.

[34] E.A. Feijani, H. Mahdavi, A. Tavasoli. Poly (vinylidene fluoride) based mixed matrix membranes comprising metal organic frameworks for gas separation applications, Chem. Eng. Res. Des. 96 (2015) 87-102. http://dx.doi.org/10.1016/j.cherd.2015.02.009.

[35] M.E. Brenchley, M.T. Weller, Structures of strontium selenite and strontium selenide aluminate sodalites and the relationship of framework structure to vibrational spectra in aluminate sodalities, Chem. Mater. 2 (1993) 1003-1005. http://dx.doi.org/10.1002/chin.199343005.

[36] D. Novembre, B.D. Sabatino, D. Gimeno, Synthesis and characterization of Na-X, Na-A and Na-P zeolites and hydroxysodalite from metakaolinite, Clay. Miner. 46 (2011) 339-354. http://dx.doi.org/10.1180/claymin.2011.046.3.339.

[37] W.H. Lin, R.H. Vora, T.S. Chung, Gas transport properties of 6FDA-Durene/1,4-phenylenediamine (pPDA) copolyimides, J. Polym. Sci. Pol.

Phys. 38 (2015) 2703–2713. http://dx.doi.org/10.1002/1099-0488(20001101)38.

[38] H. Guo, G. Kong, G. Yang G, Cross-Linking between Sodalite Nanoparticles and Graphene Oxide in Composite Membranes to Trigger High Gas Permeance, Selectivity, and Stability in Hydrogen Separation, Angew. Chem. Int. Ed. 59 (2020). http://dx.doi.org/10.1002/anie.201915797.

[39] T. C. Merkel, M. Zhou, R.W. Baker, Carbon dioxide capture with membranes at an IGCC power plant, J. Membr. Sci. 389 (2012) 441-450. http://dx.doi.org/10.1016/j.memsci.2011.11.012.